Decoupled spin crossover and structural phase transition in a molecular iron(II) complex

Laurence J. Kershaw Cook, Helena Shepherd, Tim P. Comyn, Chérif Baldé, Oscar Cespedes, Guillaume Chastanet, Malcolm A Halcrow

Decoupled spin crossover and structural phase transition in a molecular iron(II) complex

Laurence J. Kershaw Cook[1] , Helena J. Shepherd[2] , Tim P. Comyn[3] , Chérif Baldé[4,5] , Oscar Cespedes[6] , Guillaume Chastanet[5] , Malcolm A. Halcrow[1]

[1] *School of Chemistry, University of Leeds, Woodhouse Lane, Leeds, LS2 9JT (UK), Fax: (+44) 113-343-6565.*
[2] *Department of Chemistry, University of Bath, Claverton Down, Bath BA2 7AY (UK).*
[3] *Institute for Materials Research, School of Chemical and Process Engineering, University of Leeds, Leeds, LS2 9JT (UK).*
[4] *University of Ziguinchor, Sciences and Technology Department, 253 Ziguinchor (Senegal).*
[5] *CNRS, Univ. Bordeaux, ICMCB, UPR 9048, F-33600 Pessac (France)*
[6] *School of Physics and Astronomy, University of Leeds, E.C. Stoner Building, Leeds, LS2 9JT (UK)*

Corresponding author(s) : m.a.halcrow@leeds.ac.uk / guillaume.chastanet@icmcb.cnrs.fr

Supporting information available on the publisher web site

Abstract : Crystalline $[Fe(bppSMe)_2][BF_4]_2$ (**1**; bppSMe=4-(methylsulfanyl)-2,6-di(pyrazol-1-yl)pyridine) undergoes an abrupt spin-crossover (SCO) event at 265±5 K. The crystals also undergo a separate phase transition near 205 K, involving a contraction of the unit-cell *a* axis to one-third of its original value (high-temperature phase 1; *Pbcn*, *Z*=12; low-temperature phase 2; *Pbcn*, *Z*=4). The SCO-active phase 1 contains two unique molecular environments, one of which appears to undergo SCO more gradually than the other. In contrast, powder samples of **1** retain phase 1 between 140–300 K, although their SCO behaviour is essentially identical to the single crystals. The compounds $[Fe(bppBr)_2][BF_4]_2$ (**2**; bppBr=4-bromo-2,6-di(pyrazol-1-yl)pyridine) and $[Fe(bppI)_2][BF_4]_2$ (**3**; bppI=4-iodo-2,6-di(pyrazol-1-yl)-pyridine) exhibit more gradual SCO near room temperature, and adopt phase 2 in both spin states. Comparison of **1**–**3** reveals that the more cooperative spin transition in **1**, and its separate crystallographic phase transition, can both be attributed to an intermolecular steric interaction involving the methylsulfanyl substituents. All three compounds exhibit the light-induced excited-spin-state trapping (LIESST) effect with *T*(LIESST=70–80 K), but show complicated LIESST relaxation kinetics involving both weakly cooperative (exponential) and strongly cooperative (sigmoidal) components.

Introduction

The structural chemistry of molecular spin-crossover (SCO) materials[1–4] continues to be of great interest, for two reasons.[5, 6] One, is to elucidate the factors underlying cooperative spin-state switching so that new materials with useful switching properties can be designed for nanoscience and device applications.[3] However, the study of SCO by multiple techniques also affords more general information about the underlying chemistry of crystallographic phase transitions, which is important for the crystal engineering of other types of functional material. Increasingly complex structural behaviour is being reported in spin-transition crystals,[5] including: stepwise spin transitions coupled to multiple crystallographic phase changes;[7, 8] incomplete SCO reflecting symmetry-breaking transitions generating a mixture of active and inactive sites in a material;[9] and, thermal hysteresis induced by large changes in molecular conformation during SCO, rather than a change in crystallographic symmetry.[10]

We report here $[Fe(bppSMe)_2][BF_4]_2$ (**1**; bppSMe=4-(methyl-sulfanyl)-2,6-di(pyrazol-1-yl)pyridine), whose crystals exhibit a thermal spin transition near room temperature that is decoupled from a crystallographic phase change at lower temperature. Only two other SCO materials show comparable behaviour: $[\{Fe(NCS)_2(3\text{-bpp})\}_2(\mu\text{-}4,4'\text{-bipy})]$ (3-bpp=2,6-di(pyrazol-3-yl)pyridine; 4,4'-bipy=4,4'-bipyridyl)[11] and $[FeL_2][BF_4]_2$ (L=2,6-di(5-methylpyrazol-3-yl)pyridine),[12] which both undergo one or more crystallographic phase changes above their spin-transition

temperatures. Two other complexes $[Fe(bppBr)_2][BF_4]_2$ (**2**; bppBr=4-bromo-2,6-di(pyrazol-1-yl)pyridine) and $[Fe(bppI)_2][BF_4]_2$ (**3**; bppI=4-iodo-2,6-di(pyrazol-1-yl)pyridine)13 are also described, which are isostructural to **1** at low temperature, but do not exhibit the crystallographic phase change. Comparison of these compounds has allowed us to identify the intermolecular interactions in **1** that cause its more complicated SCO and phase behaviour, and has thus afforded a structure–function relationship for SCO in this type of crystal lattice.

Results and Discussion

The ligands bppBr and bppI14 were both obtained from 4-amino-2,6-di(pyrazol-1-yl)pyridine ($bppNH_2$)14 by a diazotisation procedure. Treatment of bppI with NaSH in DMF affords 4-mercapto-2,6-di(pyrazol-1-yl)pyridine (bppSH),15 which was methylated with MeI to give bppSMe, together with the disulfides bppSSbpp15 and bppSSMe (Scheme 1). Pure bppSMe can be isolated from the mixture by vacuum sublimation, whereas the disulfido products were purified from the involatile residue by silica column chromatography. Complexation of hydrated $Fe[BF_4]_2$ with 2 equivalents of the appropriate ligand in nitromethane yielded the complex salts **1**–**3**, which all form solvent-free yellow crystals from nitromethane/diethyl ether mixtures.16

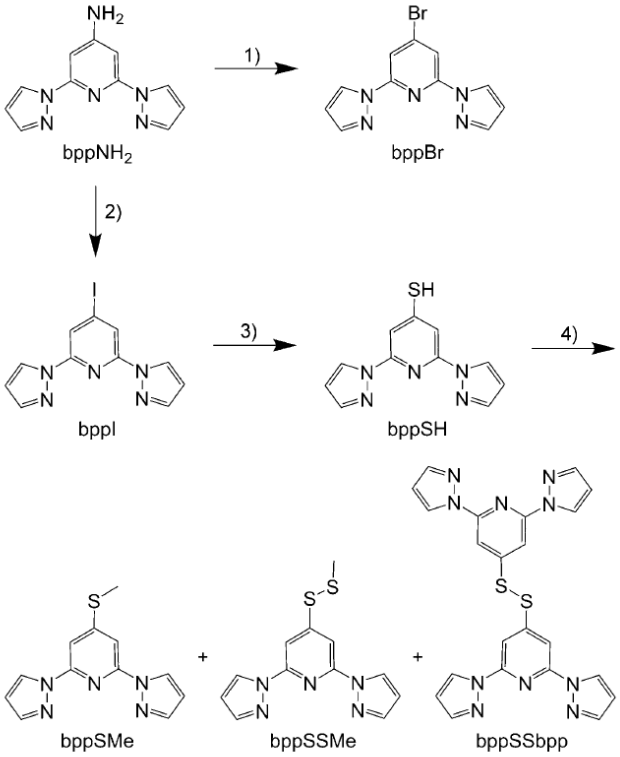

Scheme 1. Synthesis of the ligands in this study. Conditions used: 1) $NaNO_2$, KBr, HBr (aq), MeCN, RT→reflux then $Na_2S_2O_3$ (aq); 2) Isopentyl nitrite, KI, I_2, CH_2Cl_2, RT→reflux then $Na_2S_2O_3$ (aq);[14] 3) NaSH, DMF, reflux;[15] 4) MeI, K_2CO_3, MeCN, 85 °C.

The variable-temperature magnetic susceptibility of a powder sample of **1** demonstrated a thermal spin transition with a small thermal hysteresis width of 2 K ($T_{1/2}\downarrow$=268 K, $T_{1/2}\uparrow$=270 K; Figure 1). Although the transition has no discontinuities at first glance, only about 80 % of the sample is in the low-spin state at 250 K ($\chi_M T$=0.7 $cm^3\ mol^{-1}$ K) with the remainder of the material becoming low spin more gradually on further cooling. The first derivative of the susceptibility curve shows the transition is not symmetrical, and contains small discontinuities near 220 and 330 K (Figure 1).17 Therefore, SCO in **1** appears to contain two components: an abrupt, hysteretic transition undergone by about 70 % of the sample; and, a more gradual crossover with a similar midpoint temperature, involving the remaining 30 %. That suggestion is also supported by the differential scanning calorimetry (DSC) data described below. In contrast, **2** and **3** both exhibit more gradual SCO, with no masked features in their $\delta(\chi_M T)/\delta T$ curves and midpoint temperatures of $T_{1/2}$=307 K (**2**) and 332 K (**3**). The SCO cooperativity, as measured by the maximum value

of $\delta(\chi_M T)/\delta T$, follows the order **1**>**3**>**2** (Figure 1). The SCO transition for **3** is essentially identical to that shown by the perchlorate salt of the same complex.[13]

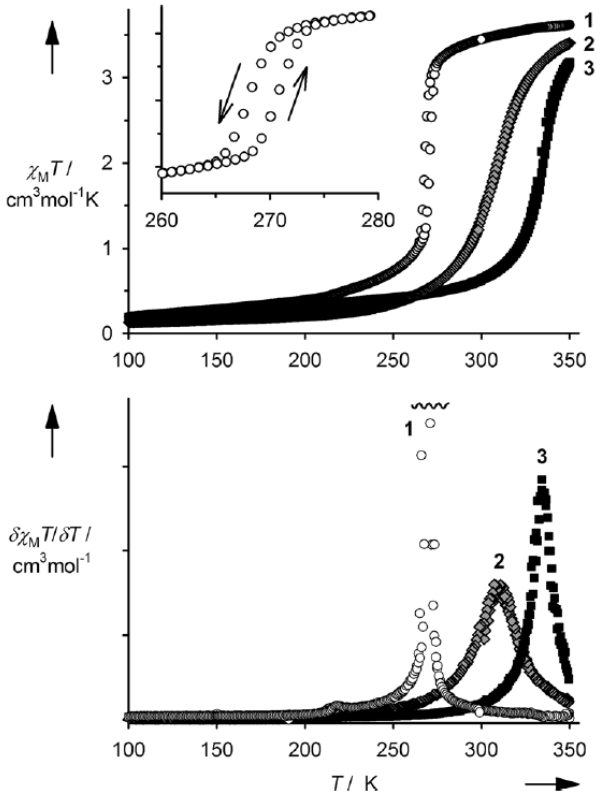

Figure 1. Top: variable-temperature magnetic susceptibility data for **1** (○), **2** (◆) and **3** (■), measured with a 298→350→3→298 K temperature ramp. The inset shows the thermal hysteresis on the abrupt part of the spin transition of **1**. Bottom: the first derivative of the $\chi_M T$ versus T curves of **1** (○), **2** (◆) and **3** (■).[17]

Initial structure refinements showed that **1**–**3** are isostructural in the single crystal at 100 K, in the space group *Pbcn*. Their asymmetric units contain half a complex cation with crystallographic C_2 symmetry, and one unique BF_4^- ion (Figure 2). The iron centres are all low spin at this temperature, and show only small deviations from the idealised D_{2d} symmetry that is expected with this ligand type (Table 1). The complex cations pack in layers in the crystals, related to the "terpyridine embrace" lattice that is often adopted by salts of $[Fe(bpp)_2]^{2+}$ derivatives.[12, 18–20] The cation layers in the full embrace structure have strict or approximate four-fold symmetry, with each molecule interdigitating to four nearest neighbours through face-to-face and edge-to-face π–π interactions between their pyrazolyl rings.[21] In **1**–**3**, although the layered structure is retained, this interdigitation is disrupted by the pyridyl substituents, which protrude into the adjacent layers (Figure 3). Thus, each $[Fe(bppR)_2]^{2+}$ cation (R=SMe, Br or I) experiences a partial terpyridine embrace, forming just two intra-layer π–π interactions to face-to-face pyrazolyl rings.

Unit-cell measurements showed that, in addition to SCO at 260–270 K, crystals of **1** undergo a second phase transition between 210 and 200 K, involving a contraction of the unit-cell *a* axis from 53–54 Å in the higher temperature phase (phase 1) to 18 Å in the low-temperature phase (phase 2). The spin transition near 270 K is accompanied by a sharp decrease in *a*, but has little effect on *b* or *c* (Figure 4). The resultant contraction in unit-cell volume (*V*), 260(27) Å^3 or 2.8 %, is typical for an abrupt thermal spin transition in an iron(II) complex salt.[6] The phase 1→phase 2 change around 205 K causes a small contraction in *b* as well as the aforementioned reduction in *a*, and is also reflected in a 23(6) Å^3 reduction in *V* (normalised to *Z*=4, Figure 4). Thus, the molecular packing in phase 2 of **1** is significantly more compact than the low-spin form of phase 1. Further cooling to 100 K leads to a small increase in *a*, which is offset by decreases in *b* and *c* to give the expected reduction in *V* with decreasing temperature.

Table 1. Selected bond distances [Å] and angles [°] for the different phases of the complexes. α, Σ and Θ are indices characteristic for the spin state of the complex,[5,22] whereas θ and φ are measures of the Jahn–Teller distortion sometimes shown by these iron centres in their high-spin state (see the Supporting Information).[23–25] Typical values of these parameters in $[Fe(bpp)_2]^{2+}$ derivatives are given in ref. [18].

	1				
	T = 290 K (HS-1)		T = 240 K (LS-1)		T = 100 K (LS-2)
	Half-molecule A	Molecule B	Half-molecule A	Molecule B	
Fe-N{pyridyl}	2.105(4)	2.103(4), 2.118(4)	1.930(5)	1.901(4), 1.901(5)	1.893(2)
Fe-N{pyrazolyl}	2.159(5), 2.170(5)	2.160(5)–2.168(5)	2.002(5), 2.015(5)	1.965(5)–1.980(5)	1.969(3), 1.971(2)
α	73.7(2)	73.5(4)	78.8(3)	79.9(4)	80.0(2)
Σ	148.9(7)	152.7(6)	98.7(8)	88.4(7)	87.6(4)
Θ	461	475	320	289	287
φ	178.6(3)	168.3(2)	178.6(3)	175.2(2)	174.28(15)
θ	89.04(5)	86.55(5)	88.09(4)	87.76(4)	87.23(2)

	2			**3**	
	T = 350 K (HS-2)	T = 250 K (LS-2)	T = 100 K (LS-2)	T = 350 K (HS-2)[a]	T = 100 K (LS-2)
Fe-N{pyridyl}	2.110(4)	1.896(6)	1.895(2)	2.077(4)	1.898(3)
Fe-N{pyrazolyl}	2.145(4), 2.146(5)	1.971(5), 1.976(6)	1.968(2), 1.982(2)	2.134(5), 2.147(5)	1.962(3), 1.968(3)
α	73.7(2)	80.2(3)	79.99(13)	74.6(3)	80.23(17)
Σ	148.8(6)	85.6(8)	87.1(3)	139.9(7)	84.8(4)
Θ	458	282	286	437	278
φ	175.9(2)	177.2(3)	175.62(13)	177.1(2)	177.21(18)
θ	89.64(4)	89.60(5)	87.02(2)	88.35(4)	86.98(2)

[a] The compound was ca. 85% high-spin at this temperature.

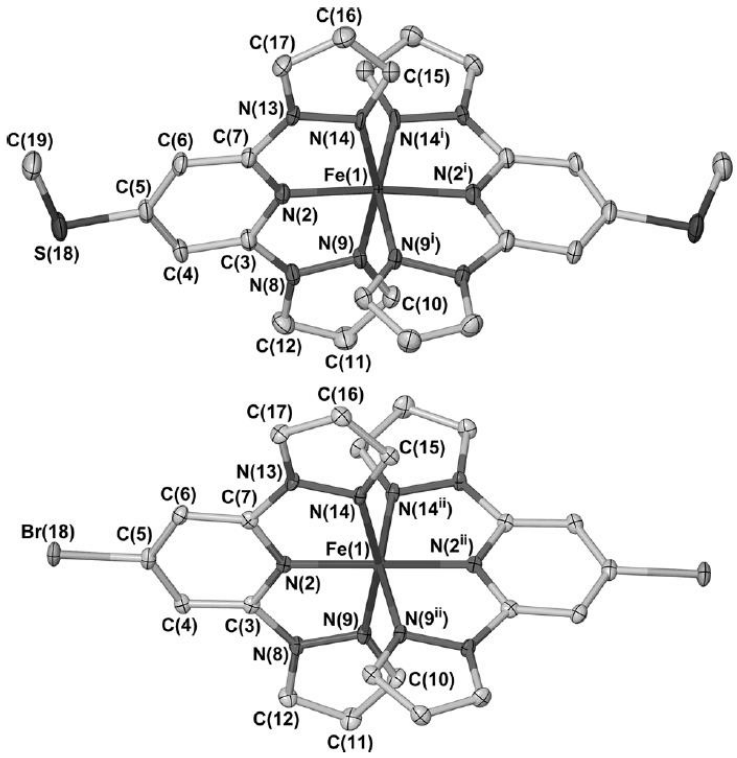

Figure 2. Views of the $[Fe(bppSMe)_2]^{2+}$ cation in **1** (top) and $[Fe(bppBr)_2]^{2+}$ in **2** (bottom) at 100 K. Displacement ellipsoids are at the 50% probability level, and all H atoms have been omitted. Symmetry codes: i) $1-x, y, {}^3/_2-z$; ii) $-x, y, {}^3/_2-z$.

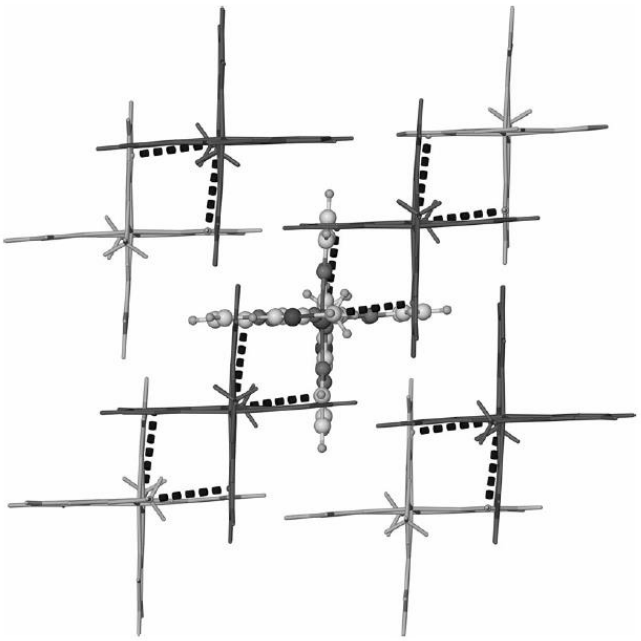

Figure 3. View of the cation layers in the LS-2 phase of **1** at 100 K. The pale coloured cations are in the same layer as the highlighted molecule, whereas the dark cations are in adjacent layers to the front and back. The close intermolecular C–H···π contacts involving the methylsulfanyl groups are also indicated. The view is perpendicular to the crystallographic (100) plane, and BF_4^- ions have been omitted for clarity.

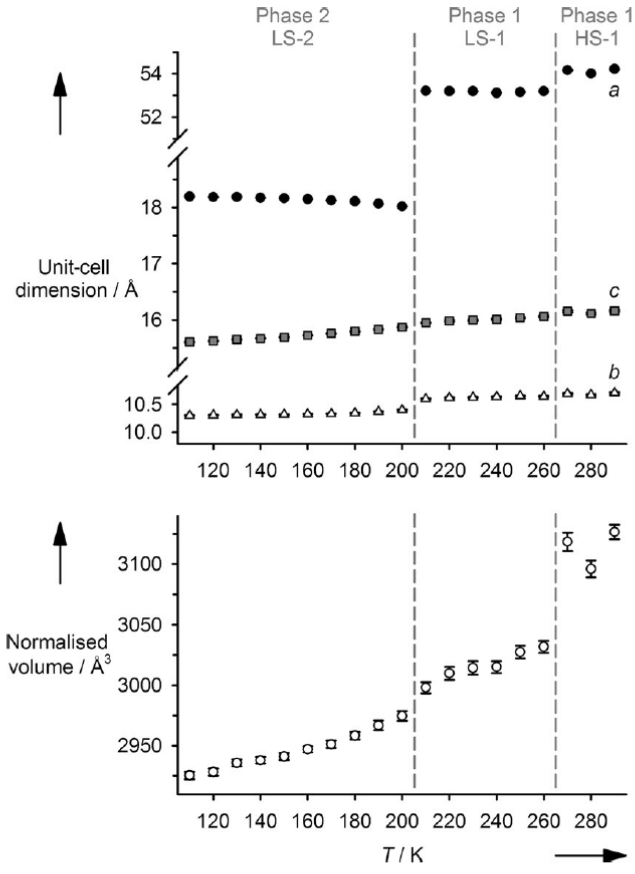

Figure 4. Temperature dependence of the single crystal unit-cell dimensions of **1** (top), and the unit-cell volume normalised to $Z=4$ (bottom), upon cooling from 290 to 110 K. Error bars are shown for all data points, but are often smaller than the symbols on the graphs.

Investigation of multiple crystals revealed that the formation of phase 1 on warming above 200–210 K was always apparent in the diffraction images, from the ingrowth of additional diffraction peaks along *a** (Figure 5). However, ingrowth of the additional reflections from phase 1 was not abrupt, and often occurred over a temperature range of 20–30 K.25 The relative intensities of the super-cell reflections, compared with the parent reflections, differed significantly between crystals, and upon repeated cycling of the same crystal.

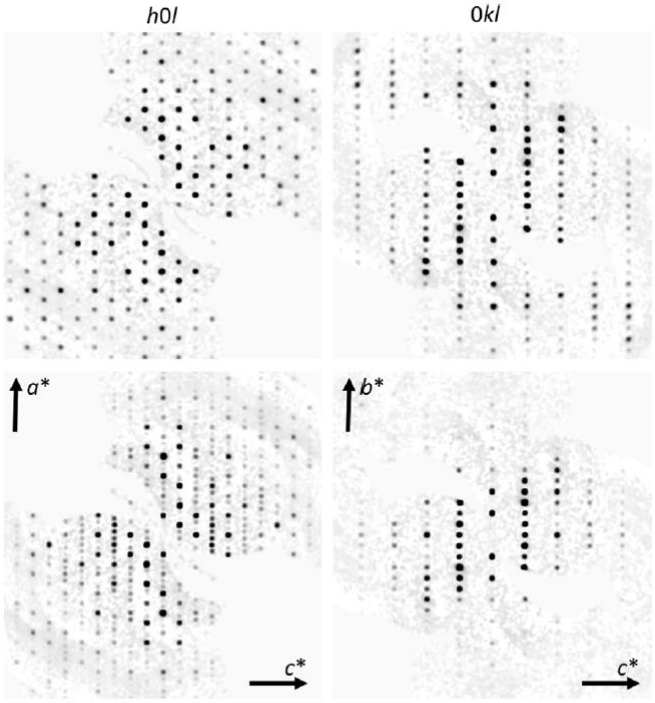

Figure 5. Diffraction images from a single crystal of **1** in the *h*0*l* and 0*kl* zones at 100 K (top) and 240 K (bottom) showing the appearance of additional reflections along *a**. The apparently weaker diffraction in *0*kl compared to *h*0*l* at 240 K is an artefact of the data reconstruction process.[25]

Although crystals of **1** always diffract well at 100 K, they often suffer from twinning above the phase 2→phase 1 transition temperature. This twinning is reversed upon re-cooling the crystals below 205 K. Hence, the formation of the phase 1 super-cell along [100] may take place in an incoherent or disordered manner in those crystals. Several attempts were required to obtain good refinements of all the phases of **1** from the same crystal. One refinement of each phase was ultimately achieved at 290 K (HS-1), 240 K (LS-1) and 100 K (LS-2); HS-1 and LS-1 are isostructural in phase 1, but in the high-spin and low-spin states, respectively. Interestingly, crystals that diffracted well at 100 K had a much higher mosaicity at 30 K, which prevented us from obtaining a useful structure of **1** at that lower temperature.

The HS-1 and LS-1 phases both contain 1.5 molecules per asymmetric unit, with a half-molecule spanning a two-fold rotation axis (molecule A) and a whole molecule on a general crystallographic site (molecule B). The iron centres are high spin in HS-1 at 290 K, and predominantly or fully low spin in LS-1 at 240 K, although there may be a residual high-spin fraction for molecule A in the latter structure (Table 1). That would be consistent with the magnetic data, which imply that about 15 % of the sample remains high spin at 240 K (Figure 1). The molecules differ in that molecule A has a more regular coordination geometry, closer to ideal D_{2d} symmetry, than molecule B. That is reflected in the *trans*-N{pyridine}-Fe-N{pyridine} angle (φ in Table 1), which is close to the expected value of 180° in molecule A (178.6(3)° in both HS-1 and LS-1), but is significantly smaller in molecule B (168.3(2) and 175.2(2)°, respectively).23, 24 Notably, φ in HS-1 molecule B is unusually low for an SCO-active complex of this type, and the change in φ during SCO for molecule B ($\Delta\varphi$=6.9(3)°) is correspondingly large.18 The greater change in shape during SCO for molecule B compared to molecule A ($\Delta\varphi$=0.0(4)°), implies that molecule B should undergo SCO more cooperatively than molecule A.5 That is consistent with the mixture of abrupt and gradual SCO evident in the susceptibility and DSC data for **1**.

The A and B cation sites in phase 1 are segregated into distinct layers in the lattice, with an ABBABB stacking pattern along the crystallographic *a* axis. Nearest-neighbour cations in the A layers are related by an inversion centre and are aligned strictly co-parallel, whereas in the B layers they are related by mirror symmetry and are slightly canted with respect to each other. This leads to an undulation of the complex molecules in adjacent layers down the [100] vector.25 In LS-2, the cation layers are all identical and equivalent to the A layers in HS-1/LS-1, and the complex molecules are all aligned linearly along [100].

The π–π interactions within the layers involve pyrazolyl rings that are strictly or approximately co-planar by symmetry and separated by 3.5 Å. The dimensions of these interactions change only slightly between the different phases of **1**.25 More variation occurs in intermolecular contacts involving the methylsulfanyl groups, however, which occupy cavities bounded by four pyrazolyl groups from two different cations in an adjacent layer. In HS-1 the intermolecular methyl···pyrazolyl distances are C···C≥3.640(14) Å, close to the sum of the van der Waals radii of a methyl group and an aromatic ring (3.7 Å).26 However, in LS-1 there is a general contraction of these interactions, and the three unique methyl groups in this structure each form one close intermolecular C-H···π contact of C···C=3.452(12), 3.531(12) and 3.573(15) Å. The shortest of these is associated with the unique methylsulfanyl group in molecule A, which exhibits a degree of disorder in the LS-1 phase. In LS-2 at 100 K, this ligand disorder is no longer apparent although the short C-H···π contact to the unique methylsulfanyl group is retained, at C···C=3.445(5) Å (Figure 3).25 Relief of this steric clash may contribute to the driving force for the LS-2→LS-1 phase change. Even though there are also several cation···anion C–H···F contacts in HS-1 and LS-1, these are less likely to contribute to the spin transition because the anions are comparably disordered in both structures.

The phase behaviour of bulk samples of **1** was probed by variable-temperature X-ray powder diffraction. Although the peaks are broad, the data show only minor changes on cooling from 300 to 140 K (Figure 6). The data at all temperatures are a better match for the simulated patterns based on phase 1 than for phase 2, particularly in the region $20 \leq 2\theta \leq 30°$ which shows the greatest difference between the two forms. Hence, in contrast to the single crystals, powder samples of **1** do not exhibit the LS-1/LS-2 transition and retain phase 1 at all accessible temperatures. This observation was supported by a DSC measurement, which showed peaks corresponding to the SCO event that are in excellent agreement with the susceptibility curve ($T\downarrow$=267 K, $T\uparrow$=270 K, ΔH=10.1(2) kJ mol^{-1}). However, no peak was observed near 205 K that could be attributed to the phase 1/phase 2 conversion, confirming that this transition does not occur in the powder sample. The measured SCO enthalpy is approximately 50 % smaller than for other compounds of the $[Fe(bpp)_2]^{2+}$ type,20, 23, 27 which is consistent with the suggestion that the abrupt part of the spin transition in **1** only involves a fraction of the iron centres in the sample (see above).

Higher-temperature crystal-structure determinations of **2** and **3** were also performed, to probe the structure changes during SCO in those materials (Table 1). In contrast to **1**, **2** and **3**, both adopt phase 2 at all the temperatures examined. Structures of **2** at 250 and 350 K, either side of the spin transition, showed it to be low spin at 250 K and high spin at 350 K, as expected from the susceptibility data (Figure 1). The metric parameters of **3** at 350 K imply a predominantly, but not fully, high-spin iron centre. That is again consistent with the susceptibility data, which predict an approximate 85 % high-spin population in the material at that temperature (Figure 1). X-ray powder diffraction confirmed that powder samples of **2** and **3** are phase pure, and adopt phase 2 as in the single crystals.

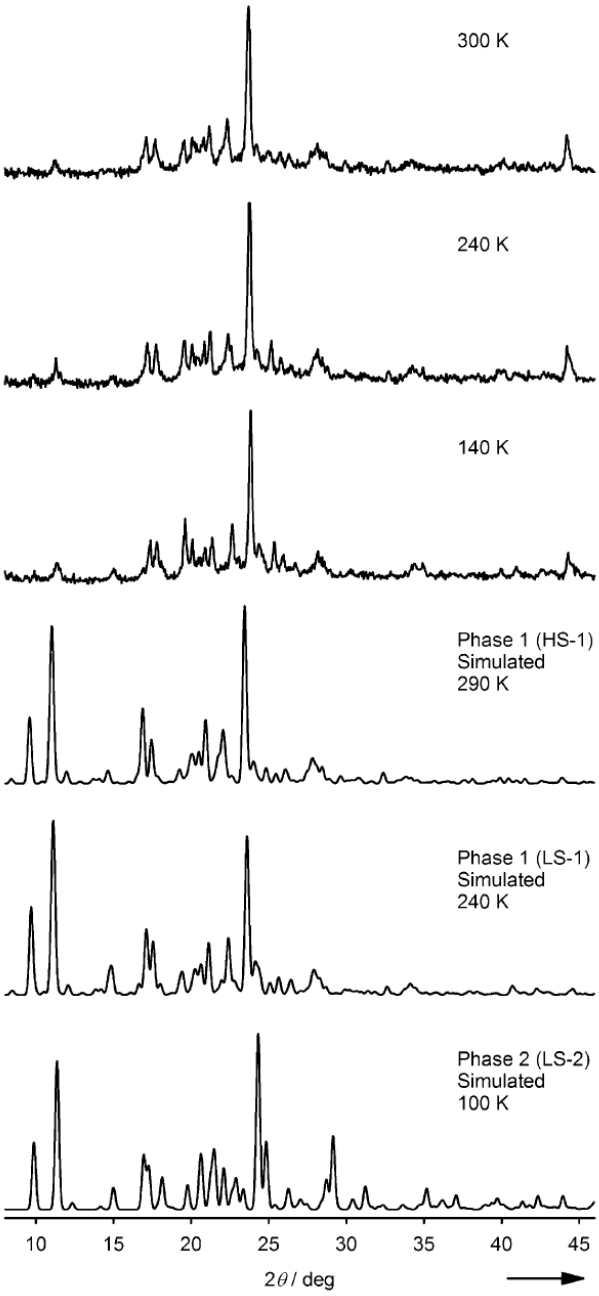

Figure 6. X-ray powder diffraction data from **1** at 300, 240 and 140 K, and simulated powder patterns based on its different crystallographic phases. The experimental data are a good match for the phase 1 simulations at all temperatures.

Salts of $[Fe(bpp)_2]^{2+}$ derivatives are well known to exhibit photomagnetic effects at low temperatures.[7, 20, 28–30] The low-spin→high-spin photo-conversion was investigated on **1**–**3** in bulk conditions by using a superconducting quantum interference device (SQUID) magnetometer coupled to a continuous waveoptical source. The samples were irradiated at the following wavelengths: 405, 510, 640, 830 and 980 nm. In each case, the most efficient wavelength to induce the LIESST effect was 510 nm, leading to a strong increase of the magnetic signal at 10 K. No reverse-LIESST was observed upon irradiation at longer wavelengths, however. By using the standardised *T*(LIESST) procedure[31, 32] we monitored the direct magnetic response on a thin layer of powders of compounds **1**–**3** upon irradiation of the $^1A_1 \rightarrow {}^1T_1$ absorption band. The *T*(LIESST) curves were then recorded for each compound (Figure 7) to determine the stabilisation of the photo-induced HS state.

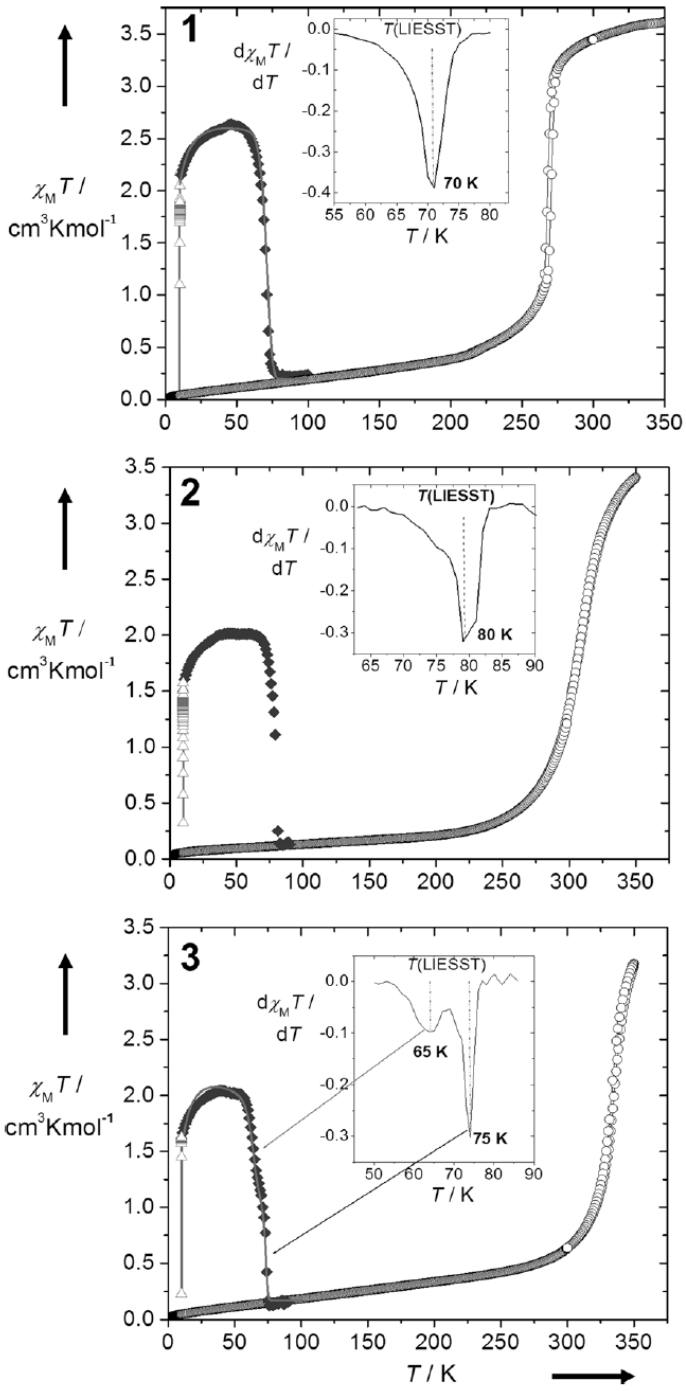

Figure 7. Temperature dependence of $\chi_M T$ for **1**–**3**: thermal behaviour of $\chi_M T$ before irradiation (○), during irradiation (Δ) at 510 nm at 10 K, and the *T*(LIESST) measurement in the warming mode when the laser was switched off (◆). The lines through the latter data for **1** and **3** show the *T*(LIESST) simulations discussed in the text. Inset: first derivative of the $\chi_M T$ versus *T* curve, recorded in the dark after irradiation, whose minimum gives *T*(LIESST).

For all complexes, a drastic increase in the magnetic signal under green-light irradiation was observed at 10 K. However, unusual for $[Fe(bpp)_2]^{2+}$ derivatives,[7, 20, 28–30] the photo-conversion efficiency was not quantitative. The maximum $\chi_M T$ values indicate photo-conversion efficiencies of 70 % (for **1**), 57 % (**2**) and 60 % (**3**). Following the irradiation procedure, an increase in $\chi_M T$ occurs upon heating from 10 K in the dark, reflecting zero-field splitting of the HS iron(II) centres.[33] For **1** and **2** the plateau reached at 40 K remains stable until 60 K, beyond which the metastable light-induced HS state rapidly decreases, reaching the baseline above 80 K. The *T*(LIESST) values can be extracted from the first derivative of the $\chi_M T$ versus *T* curves (Figure 7, inset) affording *T*(LIESST)=70

and 80 K, respectively. In contrast, the T(LIESST) curve for **3** clearly exhibits two steps, with two minima being resolved in the $\delta(\chi_M T)/\delta T$ versus T plot at 65 and 75 K.

These T(LIESST) values all agree well with the predicted values from Equation (1) (T_0=150 K),[31, 32] similarly to T(LIESST) values of most other $[Fe(bpp)_2]^{2+}$ derivatives that have been measured by this procedure.[20, 28]

$$T(\text{LIESST}) = T_0 - 0.3T_{1/2} \qquad (1)$$

However, although the differences are small, it is noteworthy that within this series **1** has both the lowest $T_{1/2}$ and the lowest T(LIESST) values, in apparent violation of Equation (1) and Hauser's inverse energy gap law.[34]

The dynamics of LIESST relaxation of the photo-induced HS fraction, γ_{HS}, were investigated for all three complexes in the 50–80 K temperature range where the HS–LS relaxation is thermally activated. The value of γ_{HS} was deduced from the equation $[(\chi_M T)_{h\nu} - (\chi_M T)_{LS}]/[(\chi_M T)_{HS} - (\chi_M T)_{LS}]$, in which $(\chi_M T)_{h\nu}$ is the magnetic value reached after irradiation, $(\chi_M T)_{LS}$ is the magnetic value of the initial LS state, and $(\chi_M T)_{HS}$ is the magnetic value recorded at room temperature for a fully HS state.

The relaxation behaviour for **1** deviates strongly from a single-exponential. However, the relaxation curves are not perfectly sigmoidal; whereas a fast exponential decay occurs at short timescales, a much slower process is also observed as a long tail at the end of the relaxation (Figure 8). The sigmoidal shape of the relaxation curves is consistent with the cooperative thermal spin transition, whereas the superimposed exponential decay reflects either the presence of short-range interactions in the lattice, or the presence of more than one relaxing species. The latter suggestion is consistent with the presence of two different iron centres in phase 1 of the sample, as predicted by the powder-diffraction data, but it could also imply a crystallographic phase 1↔2 transition occurring during the relaxation process. Therefore, the relaxation curves were simulated according to Hauser's self-acceleration model, which reflects the change in the energy barrier as a function of γ_{HS} in cooperative SCO materials.[35] [Eq. (2) and (3), with $\alpha = E_a^*/k_B T$ and $k_{HL} = k_\infty \exp(-E_a/k_B T)$]:

$$\frac{\partial \gamma_{HS}}{\partial t} = -k^*_{HL}\gamma_{HS} \qquad (2)$$

$$k^*_{HL}(T,\gamma_{HS}) = k_{HL}(T)\exp[\alpha(T)(1-\gamma_{HS})] \qquad (3)$$

This procedure yielded the solid lines shown in Figure 8. From these simulations, an Arrhenius plot can be drawn to extract the dynamical parameters E_a=1040 cm^{-1}, E_a^*=120 cm^{-1} and k_∞=6.9 10^5 s^{-1}. However the second, minor exponential component of the decay curves is clearly not reproduced by the simulation.

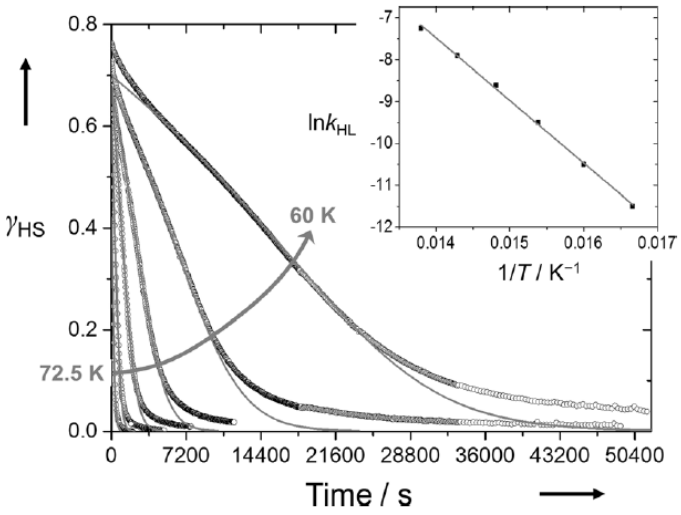

Figure 8. HS→LS relaxation for **1** at 72.5, 70, 67.5, 65, 62.5 and 60 K. The relaxation curves are fitted according to Hauser's sigmoidal law.[34] Inset: Arrhenius plot of lnk_{HL} versus 1/T. The line represents the best linear fit.

The HS–LS relaxation curves for **2** exhibit a clear multistep character (Figure 9). On the basis of the gradual, single-step, thermal SCO exhibited by **2** (Figure 1), and the single minimum in its T(LIESST) curve (Figure 7), a single-exponential or even stretched-exponential decay might have been expected. This is clearly not the case, however. Some of the relaxation steps exhibit a sigmoidal shape, indicating the presence of cooperative phases in the powder, which can be explained by the formation of domains during the relaxation process.36 The simultaneous, coincident, relaxation processes exhibited by **2** could not be accurately simulated, and we were unable to describe its global LIESST relaxation.

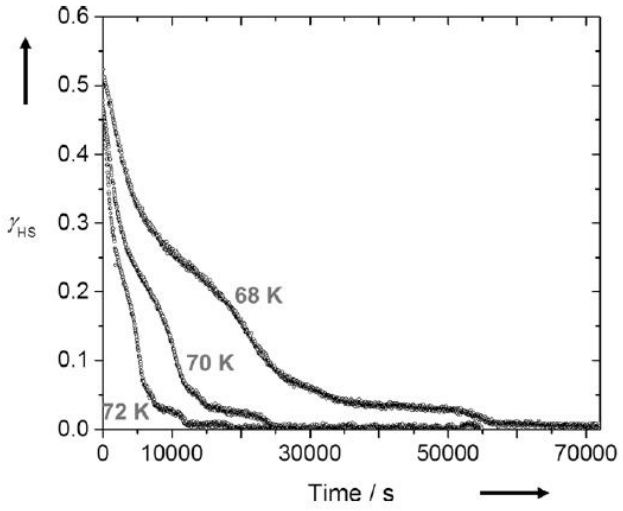

Figure 9. HS→LS relaxation at different temperatures for **2**.

Compound **3** clearly exhibits a two-step relaxation behaviour, from the shape of the T(LIESST) curve (Figure 7). The first step follows a single-exponential decay, whereas the second step exhibits a sigmoidal shape. If the relaxation process is [HS–HS]→[HS–LS]→[LS–LS], as observed in dinuclear systems,37 the second relaxation step depends on the lifetime of the first one, and the relaxation kinetics should account for this dependence. On the other hand, if the relaxation processes arise from two independent metastable sites, the two relaxation rates are not correlated.38 This latter situation seems more appropriate to describe the two-step relaxation of **3**, especially, because the two processes have sufficiently different timescales to be treated separately. By inspection, the

relaxation processes have approximately the following proportions: 40 % of exponential decay and 60 % of self-accelerating process. The first component was modelled with an exponential model, and the second part was simulated by Equation (2) and (3). Figure 10 presents the simulation obtained from this approach, leading to the dynamic parameters extracted from the ln($k_{HL}(T)$) versus 1/T plot (Figure 10, inset). For the exponential relaxation E_a=840 cm^{-1} and k_∞=4.6×10^5 s^{-1}; and for the sigmoidal simulation E_a=1140 cm^{-1}, E_a*=190 cm^{-1} and k_∞=2.2×10^6 s^{-1}. The latter values are comparable to those obtained for **1**, reflecting the similar structural environment observed for both complexes.

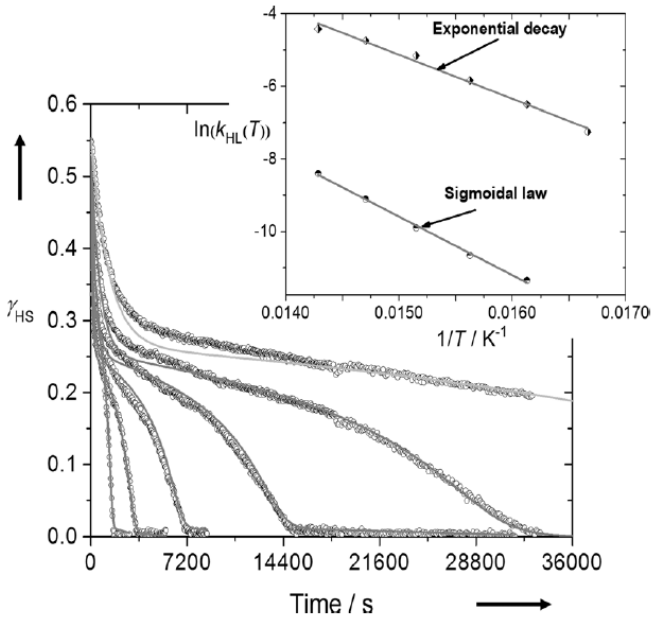

Figure 10. HS→LS relaxation for **3** at 70, 68, 66, 64, 62 and 60 K (from left to right). The relaxation curves are fitted by combining the exponential and sigmoidal models. Inset: Arrhenius plot of ln(k_{HL}) versus 1/T. The lines represent the best linear simulations.

An elegant way to validate the parameters obtained from the simulation of the relaxation kinetics is to reproduce the experimental T(LIESST) curves. The procedure takes careful account of the time and temperature dependencies of the relaxation, and combines the quantum mechanical tunnelling and the thermally activated regions [Eq. (4)].32, 39

$$\frac{\partial \gamma_{HS}}{\partial t} = -\gamma_{HS}\left\{k_0 + k_\infty \exp\left(-E_a/k_B T\right)\right\}. \exp[\alpha(T)(1-\gamma_{HS})] \quad (4)$$

The rate constant k_0 characterises the relaxation in the quantum tunnelling region, and is estimated as an upper limit from the last complete kinetic recorded at lowest temperature. k_0 is of the order of 2×10^{-5} s^{-1} for **1** and 4×10^{-5} s^{-1} for **3**.

The simulation of the double step in the T(LIESST) curve of **3** was obtained by considering 40 % of the sites with exponential decay and 60 % of the sites with sigmoidal relaxation, as above. The calculated T(LIESST) curves (Figure 7) show excellent agreement with the experimental T(LIESST) data, thereby supporting the validity of the derived parameters and the simulation procedure. The two-step character for **3** is well reproduced, and the position of the two T(LIESST) values is also well simulated.

The observation of distinct strongly and weakly cooperative LIESST relaxation regimes in **1** is consistent with the mixture of strongly and weakly cooperative thermal SCO observed in the susceptibility data, and the presence of two distinct molecular environments in the phase 1 crystal lattice. However, neither of those observations is true

for **2** or **3**, which still exhibit similarly complicated LIESST relaxation. Hence, that interpretation of the LIESST properties of **1** remains to be confirmed.

Conclusions

Compounds **1**–**3** are isostructural at 100 K, however, crystals of **1** undergo a crystallographic phase transition near 205 K. Thermal SCO then occurs upon further warming, centred at 270 K, without a further crystallographic phase change. The high-temperature (phase 1) and low-temperature (phase 2) structures have the same space group, but phase 1 is expanded along the unit-cell *a* direction and contains one-and-a-half unique molecules in its asymmetric unit. The expansion of the unit cell along [100] often occurs incoherently, as evidenced by frequent twinning of crystals in phase 1, which is reversed upon re-formation of phase 2 on cooling below 205 K. The phase transition may be driven by an intermolecular interaction between a ligand methyl substituent and a neighbouring pyrazolyl ring. In phase 2, all these C···C contacts are 0.25 Å shorter than the sum of the van der Waals radii for these groups. In phase 1, there are three unique equivalent contacts, which are 0.25, 0.17 and 0.13 Å shorter than the van der Waals sum at 240 K (just above the transition temperature). Hence, the phase 2→phase 1 transition leads to a partial relief of this steric crowding. Consistent with that suggestion, **2** and **3** do not exhibit comparable intermolecular steric clashes in their crystal lattices, and remain in phase 2 in both spin states between 100–350 K.

Interestingly, the crystallographic phase transition was only observed in single-crystal samples of **1**. Powder samples of **1** retain the room-temperature phase 1 between 140–300 K, according to DSC and powder diffraction. Particle size-dependent phase behaviour is well known at the nanoscale, where the structure of the bulk becomes influenced by the particle surface energy.[40, 41] Such phenomena are more unusual in macroscopic materials, however, where defect structures and domain sizes can influence the stability of crystal phases as well as surface effects.[42, 43] Notably the variable-temperature unit-cell, DSC and susceptibility data all imply that SCO proceeds similarly in single-crystalline and powdered **1**. That is reasonable, because both samples adopt phase 1 in the temperature range of the spin transition.

The SCO-active phase 1 contains one-and-a-half unique complex dications. The whole molecule undergoes a significant change in shape during SCO, as evidenced by an increase of nearly 7° in the *trans*-N(pyridine)-Fe-N(pyridine) angle (φ, Table 1), which is not exhibited by the other half-molecule in the unit cell (see figure in the Supporting Information). We have previously demonstrated that a change in molecular shape between the spin states can be correlated with cooperative SCO in $[Fe(bpp)_2]^{2+}$ derivatives.[5] Hence, this is consistent with the observation of abrupt (molecule B) and gradual (molecule A) SCO fractions, in an approximate 2:1 ratio, in the susceptibility data of **1**.

The literature compound $[Fe(bppCCH)_2][BF_4]_2$ (**4**; bppCCH=4-ethynyl-2,6-di(pyrazol-1-yl)pyridine) also adopts phase 2 in the high-spin state, but undergoes a phase change during SCO to a new low-spin phase in a different orthorhombic space group.[30, 44] Even though it occurs at a similar temperature to the compounds in this work, the spin transition in **4** is more cooperative with a 8 K hysteresis loop, reflecting the involvement of the phase change in its SCO. It is difficult to draw further comparison between **1**–**3** and **4**; this emphasises the structural complexity of the $[Fe(bpp)_2]^{2+}$ system in this particular lattice type.

The *T*(LIESST) values from **1**–**3** are in line with previous expectation,[20, 28] but the relaxation kinetics of their metastable high-spin states unexpectedly involve a mixture of weakly (exponential) and strongly (sigmoidal) cooperative regimes. The explanation for this behaviour is uncertain, given that **1**, and **2** and **3**, exhibit different phase behaviour in the temperature range that could be examined (above 100 K). One potential explanation, that bulk samples of **2** and **3** contain a mixture of crystal phases, is ruled out by the X-ray powder diffraction data (the same samples were used for both measurements). Alternatively, the complexes may undergo crystallographic phase changes on cooling below 100 K, and/or during photo-excitation at very low temperatures. The poor diffraction exhibited by crystals of **1** at 30 K is intriguing in that regard, and we are currently examining these possibilities in more detail.

Experimental Section

Instrumentation

Elemental microanalyses were performed by the University of Leeds School of Chemistry microanalytical service. Infrared spectra were obtained as Nujol mulls pressed between NaCl windows, between 600–4000 cm^{-1}, with a Nicolet Avatar 360 spectrophotometer. ^{1}H NMR spectra employed a Bruker DPX300 spectrometer operating at 300.2 MHz. UV/Vis/NIR measurements were performed with a PerkinElmer Lambda900 spectrophotometer in 1 cm quartz solution cells, between 200–3000 nm. Electrospray mass spectra (ESI MS) were obtained on a Waters ZQ4000 spectrometer, from MeCN feed solutions. All mass peaks have the correct isotopic distributions for the proposed assignments. X-ray powder diffraction measurements employed a Bruker D8 Advance A25 diffractometer, with $Cu_{K\alpha}$ radiation (λ=1.5418 Å). DSC measurements used a TA Instruments DSC Q20 calorimeter, heating at a rate of 10 K min^{-1}. The magnetic susceptibility, powder diffraction, DSC and LIESST measurements were all performed on the same samples of **1**–**3**.

Magnetic susceptibility measurements were performed on a Quantum Design SQUID/VSM magnetometer, in an applied field of 1000 or 5000 G. A diamagnetic correction for the sample was estimated from Pascal's constants;[45] a previously measured diamagnetic correction for the sample holder was also applied. Photomagnetic measurements were performed with a set of photo-diodes coupled through an optical fibre to the cavity of a MPMS-55 Quantum Design SQUID magnetometer operating at 2000 G. The powder sample was prepared in a thin layer (~0.1 mg) to promote full penetration of the irradiated light. The sample mass was obtained by comparison with the thermal spin transition curve measured on a larger, accurately weighed, polycrystalline sample. The sample was first slow cooled to 10 K, ensuring that potential trapping of HS species at low temperatures did not occur. Irradiation was carried out at a set wavelength and the power of the sample surface was adjusted to 5 mW cm^{-2}. Once photo-saturation was reached, irradiation was ceased and the temperature increased at a rate of 0.3 K min^{-1} to about 100 K and the magnetisation measured every 1 K to determine the T(LIESST) value given by the minimum of the $\delta(\chi_M T)/\delta T$ versus T curve for the relaxation.[32] The T(LIESST) value describes the limiting temperature above which the light-induced magnetic high-spin information is erased in a SQUID cavity. In the absence of irradiation, the magnetisation was also measured over the temperature range 10–290 K to follow the thermal spin transition and to obtain a low temperature baseline. Kinetic studies of LIESST relaxation were performed by irradiating the sample at 10 K until photo-saturation, then, under constant irradiation the sample was warmed to a desired temperature around the T(LIESST) region. At the desired temperature, irradiation is stopped and the decay of the magnetisation signal was followed for several hours or until complete relaxation back to the low-spin baseline.

Materials and methods

Unless otherwise stated, all reactions were carried out in air using non-pre-dried AR-grade solvents. 4-Amino-2,6-di(pyrazol-1-yl)pyridine (bppNH$_2$),[14] 4-iodo-2,6-di(pyrazol-1-yl)pyridine (bppI)[14] and 4-mercapto-2,6-di(pyrazol-1-yl)pyridine (bppSH)[15] were synthesised by the literature methods, whereas all other reagents were used as commercially supplied.

4-(Methylsulfanyl)-2,6-di(pyrazol-1-yl)pyridine (bppSMe) and 4-(methyldisulfanyl)-2,6-di(pyrazol-1-yl)pyridine (bppSSMe): Under dry anhydrous conditions, bppSH (0.20 g, 0.82 mmol) was added to a Schlenk tube containing K_2CO_3 (0.23 g, 1.64 mmol), iodomethane (0.33 g, 2.31 mmol) and activated molecular sieves (10 granules) in MeCN (25 cm^3). The mixture was heated to 85 °C for 18 h, during which the suspension became pale yellow in colour. The contents, once cooled, were diluted to 50 cm^3 with $CHCl_3$ (caution: strong odour), passed over a short silica pad and the silica washed further with 1:1 $CHCl_3$:MeCN (100 cm^3). The solvent was removed in vacuo and the yellow solid residue was redissolved in 1:2 hexane/EtOAc and filtered, before again being evaporated to dryness. The white solid bppSMe was isolated by sublimation under reduced pressure at 130 °C. Yield 78 mg, 37 %; m.p. 140–142 °C; ^{1}H NMR (300 MHz, $CDCl_3$); δ=2.64 (s, 3 H, SCH_3), 6.50 (br s, 2 H, pz H^4), 7.71 (s, 2 H, py $H^{3/5}$), 7.76 (br s, 2 H, pz H^3), 8.56 ppm (d, 2.1 Hz, 2 H, pz H^5); ^{13}C NMR (75.5 MHz, $CDCl_3$); δ=14.2 (SCH_3), 105.1 (2 C, py $C^{3/5}$), 108.0 (2 C, pz C^4), 127.3 (2 C, pz C^5), 142.3 (2 C, pz C^3), 149.8 (2 C, pz $C^{2/6}$), 156.5 ppm (1 C, py C^4); MS (ES): m/z: 280.1 $[Na(bppSMe)]^+$; elemental analysis calcd (%) for $C_{12}H_{11}N_5S$ (257.32): C 56.0, H 4.31, N 27.2; found: C 55.6, H 4.35, N 27.3.

The involatile residue from the sublimation contains the symmetric disulfides bppSSbpp15 and bppSSMe, which were separated by silica column chromatography (eluent 99:1 CH_2Cl_2/MeOH). bppSSMe (R_f 0.66) was obtained as a white solid. Yield 73 mg, 20 %; m.p. 115–117 °C; ^{1}H NMR (300 MHz, $CDCl_3$); δ=2.54 (s, 3 H, SCH_3), 6.51 (dd, 1.9 and 2.6 Hz, 2 H, pz H^4), 7.79 (d, 1.6 Hz, 2 H, pz H^3), 8.04 (s, 2 H, py $H^{3/5}$), 8.57 ppm (d, 2.6 Hz, 2 H, pz H^5); ^{13}C NMR (75.5 MHz, $CDCl_3$); δ=23.0 (SCH_3), 105.3 (2 C, py $C^{3/5}$), 108.1 (2 C, pz C^4), 127.3 (2 C, pz C^5), 142.5 (2 C, pz C^3), 150.3 (2 C, pz $C^{2/6}$), 155.1 ppm (1 C, py C^4); MS (ES): *m*/*z*: 290.1 [H(bppSSMe)]$^+$, 312.0 [Na(bppSSMe)]$^+$; elemental analysis calcd (%) for $C_{12}H_{11}N_5S_2$ (289.18): C 49.8, H 3.83, N 24.2; found: C 49.9, H 3.80, N 24.0.16

4-Bromo-2,6-di(pyrazol-1-yl)pyridine (bppBr): $bppNH_2$ (0.39 g, 1.73 mmol) and $NaNO_2$ (2.51 mg, 3.64 mmol) were suspended in MeCN (25 cm^3) under an atmosphere of N_2. Addition of KBr (0.49 g, 4.15 mmol) and 48 % aqueous HBr (10 cm^3, 59.3 mmol) caused immediate darkening of the mixture. The mixture was stirred for 1 h at room temperature, then heated to 80 °C for 1 h. The cooled mixture was poured into saturated aqueous $Na_2S_2O_3$ (100 cm^3) and shaken, precipitating a pale solid. The solid was then collected on a glass frit and washed with H_2O. Silica gel column chromatography (3:2 CH_2Cl_2/hexane eluent; R_f 0.19) yielded the product as a white solid, which was recrystallised from *n*-hexane. Yield 0.16 g, 32 %; m.p. 148–150 °C; ^{1}H NMR (300 MHz, $CDCl_3$); δ=6.52 (dd, 1.7 and 2.6 Hz, 2 H, pz H^4), 7.77 (d, 1.7 Hz, 2 H, pz H^3), 8.06 (s, 2 H, py $H^{3/5}$), 8.53 ppm (d, 2.6 Hz, 2 H, pz H^5); ^{13}C NMR (75.5 MHz, $CDCl_3$); δ=108.4 (2 C, pz C^4), 112.7 (2 C, py $C^{3/5}$), 127.3 (2 C, pz C^5), 136.7 (1 C, py C^4), 142.9 (2 C, pz C^5), 150.4 ppm (2 C, py $C^{2/6}$). MS (ES): *m*/*z* 290.0 [H(bppBr)]$^+$; elemental analysis calcd (%) for $C_{11}H_8BrN_5 \cdot 1/2H_2O$ (299.13): C 44.2, H 3.03, N 23.4; found: C 44.6, H 2.95, N 22.8.

Synthesis of complexes: The same basic method, described here for $[Fe(L^2SMe)_2][BF_4]_2$ (**1**), was used for all the complexes. A solution of bppSMe (70 mg, 0.27 mmol) and $Fe[BF_4]_2 \cdot 6\,H_2O$ (45 mg, 0.13 mmol) in nitromethane (20 cm^3) was stirred at room temperature for 1 h. The solution was filtered and concentrated to about 5 cm^3, then the product was precipitated by addition of diethyl ether. Isolated yields ranged from 87–95 %. Microanalytical data for the complexes are listed below.

$[Fe(bppSMe)_2][BF_4]_2$ (1): Calcd (%) for $C_{24}H_{22}B_2F_8FeN_{10}S_2$ (744.09): C 38.7, H 2.98, N 18.8; found: C 38.4, H 2.95, N 18.5.

$[Fe(bppBr)_2][BF_4]_2$ (2): Calcd (%) for $C_{22}H_{16}B_2Br_2F_8FeN_{10}$ (809.70): C 32.6, H 1.99, N 17.3; found: C 32.5, H 1.90, N 16.9.

$[Fe(bppI)_2][BF_4]_2$ (3): Calcd (%) for $C_{22}H_{16}B_2F_8FeI_2N_{10}$ (903.69): C 29.2, H 1.78, N 15.5; found: C 29.3, H 1.70, N 15.5.

Single-crystal structure analyses: Single crystals of **1**–**3** were all obtained by slow diffusion of diethyl ether vapour into nitromethane solutions of the compounds. Diffraction data were collected with an Agilent Supernova dual-source diffractometer fitted with Oxford Cryosystems cryostat, or with a HELIX cryostat for the measurements at 30 K (the Agilent diffractometer is modified to accept the HELIX device). Diffraction data from **1** and **2** were measured by using monochromated $Cu_{K\alpha}$ radiation (λ=1.54184 Å). Several crystals of **1** were screened to find one that diffracted sufficiently well at room temperature. That crystal was then used for all three data collections, measured in a 290→240→100 K temperature sequence. Two different crystals were used for **2**, one for the 100 K structure and the other for the two higher temperature measurements. Data for **3** were collected with the same diffractometer, but with monochromated $Mo_{K\alpha}$ radiation (λ=0.71073 Å) to avoid absorption problems. Data sets were corrected for absorption by an empirical multi-scan method, based on spherical harmonics.46 The structures were solved by direct methods (SHELXS-97),47 then developed by least-squares refinement on F^2 (SHELXL-97).47 Crystallographic figures were prepared using XSEED.48 Experimental data for the structure determinations are collected in Tables 2 and 3. The unit-cell data in Figure 4 were collected under the same conditions, with $Mo_{K\alpha}$ radiation.

Table 2. Experimental details for the crystal structure determinations of the different phases of **1** ($C_{24}H_{22}B_2F_8FeN_{10}S_2$, formula weight 744.11 g mol^{-1}, crystal system orthorhombic, space group *Pbcn*).

	HS-1	LS-1	LS-2
a [Å]	54.2154(15)	53.2503(12)	18.1992(3)
b [Å]	10.7072(6)	10.6457(4)	10.2991(2)
c [Å]	16.1589(6)	16.0369(4)	15.5914(3)
V [Å^3]	9380.2(7)	9091.1(5)	2922.38(9)
T [K]	290(2)	240(2)	100(2)
Z	12	12	4
D_{calcd} [g cm^{-3}]	1.581	1.631	1.691
μ [mm^{-1}]	5.873	6.060	6.284
Min./max. transmission	0.54/1.00	0.51/1.00	0.63/1.00
Θ_{max} [°]	67.10	67.08	73.63
Measured reflections	23 206	22 476	7466
Unique reflections	8367	8098	2878
Reflections [$Fo > 4\sigma(Fo)$]	5363	5602	2642
R_{int}	0.053	0.049	0.023
Parameter	661	652	215
R_1[a] [$Fo > 4\sigma(Fo)$]	0.082	0.081	0.049
wR_2[b] [all data]	0.257	0.241	0.137
GOF	1.056	1.035	1.063
$\Delta\rho_{max}$, $\Delta\rho_{min}$ [eÅ^{-3}]	0.90/−0.54	0.95/−0.58	1.47/−0.60

[a] $R = \Sigma[|F_o| - |F_c|]/\Sigma|F_o|$. [b] $wR = [\Sigma w(F_o^2 - F_c^2)/\Sigma wF_o^4]^{1/2}$

CCDC-1006370 http://www.ccdc.cam.ac.uk/cgi-bin/catreq.cgi (**1**, LS-2), CCDC-1006371 http://www.ccdc.cam.ac.uk/cgi-bin/catreq.cgi (**1**, LS-1), CCDC-1006372 http://www.ccdc.cam.ac.uk/cgi-bin/catreq.cgi (**1**, HS-1), CCDC-1006373 http://www.ccdc.cam.ac.uk/cgi-bin/catreq.cgi (**2**, 100 K), CCDC-1006374 http://www.ccdc.cam.ac.uk/cgi-bin/catreq.cgi (**2**, 250 K), CCDC-1006375 http://www.ccdc.cam.ac.uk/cgi-bin/catreq.cgi (**2**, 350 K), CCDC-1006376 http://www.ccdc.cam.ac.uk/cgi-bin/catreq.cgi (**3**, 100 K) and CCDC-1006377 http://www.ccdc.cam.ac.uk/cgi-bin/catreq.cgi (**3**, 350 K) contain the supplementary crystallographic data for this paper. These data can be obtained free of charge from The Cambridge Crystallographic Data Centre via www.ccdc.cam.ac.uk/data_request/cif.

Table 3. Experimental details for the crystal structure determinations of **2** ($C_{22}H_{16}B_2Br_2F_8FeN_{10}$, formula weight 809.74 g mol^{-1}, crystal system orthorhombic, space group *Pbcn*) and **3** ($C_{22}H_{16}B_2F_8I_2FeN_{10}$, formula weight 903.72 g mol^{-1}, crystal system orthorhombic, space group *Pbcn*).

	2[a]			**3**[b]	
	HS-2	LS-2	LS-2	HS-2[c]	LS-2
a [Å]	17.2631(5)	17.5486(9)	17.8625(3)	17.4698(9)	16.8364(4)
b [Å]	10.4120(5)	9.9817(9)	9.3666(2)	10.6631(9)	11.1465(5)
c [Å]	16.6989(8)	16.4985(11)	16.5749(3)	16.6117(11)	15.5406(5)
V [Å^3]	3001.5(2)	2890.0(4)	2773.16(9)	3094.5(4)	2916.46(18)
T [K]	350(2)	250(2)	100(2)	350(2)	100(2)
Z	4	4	4	4	4
D_{calcd} [g cm^{-3}]	1.792	1.861	1.939	1.940	2.058
μ [mm^{-1}]	7.914	8.220	8.566	2.564	2.720
Min./max. transmission	0.76/1.00	0.50/1.00	0.61/1.00	0.65/1.00	0.84/1.00
Θ_{max} [°]	72.05	71.92	74.03	29.82	26.37
Measured reflections	5966	5624	10444	15927	15286
Unique reflections	2854	2735	2768	3916	2976
Reflections [$Fo > 4\sigma(Fo)$]	1820	2006	2541	1734	2445
R_{int}	0.031	0.038	0.047	0.056	0.065
Parameter	233	233	204	233	204
R_1[d] [$Fo > 4\sigma(Fo)$]	0.060	0.077	0.035	0.055	0.032
wR_2[e] [all data]	0.172	0.231	0.090	0.163	0.072
GOF	1.050	1.070	1.050	1.029	1.051
$\Delta\rho_{max}$, $\Delta\rho_{min}$ [eÅ^{-3}]	0.34/−0.48	0.97/−1.23	0.63/−1.17	0.40/−0.63	0.83/−0.68

[a] Data collected using $Cu_{K\alpha}$ radiation. [b] Data collected by $Mo_{K\alpha}$ radiation. [c] The compound was ca. 85 % high-spin at this temperature. [d] $R = \Sigma[|F_o| - |F_c|]/\Sigma|F_o|$. [e] $wR = [\Sigma w(F_o^2 - F_c^2)/\Sigma wF_o^4]^{1/2}$

Structure refinement of 1 (HS-1): The asymmetric unit contains 1.5 formula units, with half a complex cation spanning the C_2 axis 1/2, *y*, 3/4 (molecule A); and, a whole complex dication (molecule B) and three unique BF_4^- anions lying on general crystallographic sites. All three anions are disordered over two or three sites, each sharing a common wholly occupied B atom, which results in some significant deviations from a tetrahedral structure. The refined restraints B-F=1.37(2) and F···F=2.24(2) Å were applied to these residues. All wholly occupied non-H atoms were refined anisotropically, and all H atoms were placed in calculated positions and refined by using a riding model.

Structure refinement of 1 (LS-1): This structure is isostructural with HS-1, and its refinement showed only two significant differences from the previous one. First, there is a slightly different pattern of disorder in the three unique anions. The second difference is the resolution of a minor, 15 %-occupied, disorder site for the methylsulfanyl group of half-molecule A, which was refined by using the fixed restraint C□S=1.78(2) Å. All wholly occupied non-H atoms plus the major methylsulfanyl disorder orientation were refined anisotropically, and all H atoms were placed in calculated positions and refined using a riding model.

Structure refinement of 1 (LS-2): This asymmetric unit contains half a formula unit, with Fe(1) lying on the crystallographic C_2 axis 1/2, *y*, 3/4 and one unique BF_4^- ion on a general crystallographic site. No disorder was detected during refinement, and no restraints were applied. All non-H atoms were refined anisotropically, whereas H atoms were placed in calculated positions and refined by using a riding model. The highest residual Fourier peak of +1.5 e Å^{-3} is 1.2 Å from S(18), and may reflect a remnant of the disorder in that group that is present in molecule A of the LS-1 refinement.

Structure refinements of 2: The asymmetric unit contains half a formula unit, with Fe(1) spanning the crystallographic C_2 axis 0, *y*, 3/4. The unique BF_4^- ion is badly disordered at 250 and 350 K, and was refined over four equally occupied orientations that share a common full-occupancy B atom. The resultant partial anions deviate significantly from a tetrahedral structure. The refined restraints B□F=1.39(2) and F···F=2.27(2) Å were applied to the disordered anion. At 100 K this disorder was no longer apparent, and the anion was modelled without restraints

at that temperature. All non-H atoms except the disordered F atoms (where applicable) were refined anisotropically, and H atoms were placed in calculated positions and refined by using a riding model.

Structure refinements of 3: The asymmetric unit contains half a formula unit, with Fe(1) lying on the crystallographic C_2 axis 1/2, *y*, 3/4. No disorder was present in the model at 100 K, but at 350 K the unique BF_4^- site is disordered and was refined over four equally occupied orientations that share a common full-occupancy B atom. The resultant partial anions deviate significantly from a tetrahedral geometry. The refined restraints B-F=1.40(2) and F···F=2.28(2) Å were applied to the disordered anion. All non-H atoms except the disordered F atoms (where applicable) were refined anisotropically, and H atoms were placed in calculated positions and refined by using a riding model.

Acknowledgements

This work was funded by the EPSRC (EP/H015639/1, EP/K012576/1 and EP/K00512X/1). The Aquitaine Region is acknowledged for the development of the International Centre of Photomagnetism in Aquitaine (ICPA) platform.

References

1 Spin Crossover in Transition Metal Compounds I–III, Top. Curr. Chem. (Eds.:), Springer, New York, 2004, pp. 233– 235.

2 Spin-Crossover Materials—Properties and Applications (Ed.:), Wiley, Chichester, 2013, p. 568.

3 - 3aA. Bousseksou, G. Molnár, L. Salmon, W. Nicolazzi, *Chem. Soc. Rev.* 2011, 40, 3313– 3335; 3bH. J. Shepherd, G. Molnár, W. Nicolazzi, L. Salmon, A. Bousseksou, *Eur. J. Inorg. Chem.* 2013, 653– 661.

4 - For other recent reviews see: 4aP. Gamez, J. S. Costa, M. Quesada, G. Aromí, *Dalton Trans.* 2009, 7845– 7853; 4bM. Carmen Muñoz, J. A. Real, *Coord. Chem. Rev.* 2011, 255, 2068– 2093; 4cJ. Tao, R.-J. Wei, R.-B. Huang, L.-S. Zheng, *Chem. Soc. Rev.* 2012, 41, 703– 737; 4dP. Gütlich, *Eur. J. Inorg. Chem.* 2013, 581– 591; 4eM. Sorai, Y. Nakazawa, M. Nakano, Y. Miyazaki, *Chem. Rev.* 2013, 113, PR 41–PR 122.

5 M. A. Halcrow, *Chem. Soc. Rev.* 2011, 40, 4119– 4142.

6 P. Guionneau, *Dalton Trans.* 2014, 43, 382– 393.

7 - 7aV. A. Money, C. Carbonera, J. Elhaïk, M. A. Halcrow, J. A. K. Howard, J.-F. Létard, *Chem. Eur. J.* 2007, 13, 5503– 5514; 7bM. Nihei, H. Tahira, N. Takahashi, Y. Otake, Y. Yamamura, K. Saito, H. Oshio, *J. Am. Chem. Soc.* 2010, 132, 3553– 3560.

8 - 8aD. Chernyshov, M. Hostettler, K. W. Törnroos, H.-B. Bürgi, *Angew. Chem. Int. Ed.* 2003, 42, 3825– 3830; *Angew. Chem.* 2003, 115, 3955– 3960; 8bS. Bonnet, M. A. Siegler, J. S. Costa, G. Molnár, A. Bousseksou, A. L. Spek, P. Gamez, J. Reedijk, *Chem. Commun.* 2008, 5619– 5621; 8cN. Bréfuel, H. Watanabe, L. Toupet, J. Come, N. Matsumoto, E. Collet, K. Tanaka, J.-P. Tuchagues, *Angew. Chem. Int. Ed.* 2009, 48, 9304– 9307; *Angew. Chem.* 2009, 121, 9468– 9471; 8dN. Bréfuel, E. Collet, H. Watanabe, M. Kojima, N. Matsumoto, L. Toupet, K. Tanaka, J.-P. Tuchagues, *Chem. Eur. J.* 2010, 16, 14060– 14068; 8eM. Buron-Le Cointe, N. O. Moussa, E. Trzop, A. Moréac, G. Molnár, L. Toupet, A. Bousseksou, J. F. Létard, G. S. Matouzenko, *Phys. Rev. B* 2010, 82, 214106; 8fM. Griffin, S. Shakespeare, H. J. Shepherd, C. J. Harding, J.-F. Létard, C. Desplanches, A. E. Goeta, J. A. K. Howard, A. K. Powell, V. Mereacre, Y. Garcia, A. D. Naik, H. Müller-Bunz, G. G. Morgan, *Angew. Chem. Int. Ed.* 2011, 50, 896– 900; *Angew. Chem.* 2011, 123, 926– 930; 8gN. F. Sciortino, K. R. Scherl-Gruenwald, G. Chastanet, G. J. Halder, K. W. Chapman, J.-F. Létard, C. J. Kepert, *Angew. Chem. Int. Ed.* 2012, 51, 10154– 10158; *Angew. Chem.* 2012, 124, 10301– 10305; 8hZ.-Y. Li, J.-W. Dai, Y. Shiota, K. Yoshizawa, S. Kanegawa, O. Sato, *Chem. Eur. J.* 2013, 19, 12948– 12952; 8iJ. Kusz, M. Nowak, P. Gütlich, *Eur. J. Inorg. Chem.* 2013, 832– 842; 8jB. J. C. Vieira, J. T. Coutinho, I. C. Santos, L. C. J. Pereira, J. C. Waerenborgh, V. da Gama, *Inorg. Chem.*

2013, 52, 3845– 3850; 8kK. D. Murnaghan, C. Carbonera, L. Toupet, M. Griffin, M. M. Dîrtu, C. Desplanches, Y. Garcia, E. Collet, J.-F. Létard, G. G. Morgan, *Chem. Eur. J.* 2014, 20, 5613– 5618.

9 - 9aD. L. Reger, C. A. Little, V. G. Young, Jr., M. Pink, *Inorg. Chem.* 2001, 40, 2870– 2874; 9bM. Yamada, H. Hagiwara, H. Torigoe, N. Matsumoto, M. Kojima, F. Dahan, J.-P. Tuchagues, N. Re, S. Iijima, *Chem. Eur. J.* 2006, 12, 4536– 4549; 9cA. Lennartson, A. D. Bond, S. Piligkos, C. J. McKenzie, *Angew. Chem. Int. Ed.* 2012, 51, 11049– 11052; *Angew. Chem.* 2012, 124, 11211– 11214.

10 - 10aH. J. Shepherd, T. Palamarciuc, P. Rosa, P. Guionneau, G. Molnár, J.-F. Létard, A. Bousseksou, *Angew. Chem. Int. Ed.* 2012, 51, 3910– 3914; *Angew. Chem.* 2012, 124, 3976– 3980; 10bG. A. Craig, J. S. Costa, S. J. Teat, O. Roubeau, D. S. Yufit, J. A. K. Howard, G. Aromí, *Inorg. Chem.* 2013, 52, 7203– 7209.

11 - 11aD. Fedaoui, Y. Bouhadja, A. Kaiba, P. Guionneau, J.-F. Létard, P. Rosa, *Eur. J. Inorg. Chem.* 2008, 1022–1026; 11bA. Kaiba, H. J. Shepherd, D. Fedaoui, P. Rosa, A. E. Goeta, N. Rebbani, J. F. Létard, P. Guionneau, *Dalton Trans.* 2010, 39, 2910– 2918; 11cH. J. Shepherd, P. Rosa, L. Vendier, N. Casati, J.-F. Létard, A. Bousseksou, P. Guionneau, G. Molnár, *Phys. Chem. Chem. Phys.* 2012, 14, 5265– 5271.

12 - 12aT. D. Roberts, F. Tuna, T. L. Malkin, C. A. Kilner, M. A. Halcrow, *Chem. Sci.* 2012, 3, 349– 354; 12bT. D. Roberts, M. A. Little, F. Tuna, C. A. Kilner, M. A. Halcrow, *Chem. Commun.* 2013, 49, 6280– 6282.

13 The salt $[Fe(bppI)_2][ClO_4]_2$ has been reported previously. It is isostructural with **2** and **3** and shows a similarly gradual SCO in the solid state, with $T_{1/2}$=333 K. N. T. Madhu, I. Salitros, F. Schramm, S. Klyatskaya, O. Fuhr, M. Ruben, *C. R. Chim.* 2008, 11, 1166– 1174.

14 C. Rajadurai, F. Schramm, S. Brink, O. Fuhr, M. Ghafari, R. Kruk, M. Ruben, *Inorg. Chem.* 2006, 45, 10019–10021.

15 L. J. Kershaw Cook, J. Fisher, L. P. Harding, M. A. Halcrow, submitted for publication.

16 The complex salt $[Fe(bppSSMe)_2][BF_4]_2$ is low spin at room temperature but undergoes a spin transition on warming, with an unusual structured hysteresis loop. Structural studies on this material are in progress, and will be reported separately.

17 Although they occur at comparable temperatures, the discontinuity at 220 K in the $\delta(\chi_M T)/\delta T$ curve for **1** cannot correspond to the phase 1→phase 2 transition. The same sample was also used for the powder diffraction and DSC measurements, where the phase 1→phase 2 transformation was not observed.

18 - 18aM. A. Halcrow, *Coord. Chem. Rev.* 2009, 253, 2493– 2514; 18bL. J. Kershaw Cook, R. Mohammed, G. Sherborne, T. D. Roberts, S. Alvarez, M. A. Halcrow, *Coord. Chem. Rev.*

19 R. Pritchard, C. A. Kilner, M. A. Halcrow, *Chem. Commun.* 2007, 577– 579.

20 - 20aR. Pritchard, H. Lazar, S. A. Barrett, C. A. Kilner, S. Asthana, C. Carbonera, J.-F. Létard, M. A. Halcrow, *Dalton Trans.* 2009, 6656– 6666; 20bR. Mohammed, G. Chastanet, F. Tuna, T. L. Malkin, S. A. Barrett, C. A. Kilner, J.-F. Létard, M. A. Halcrow, *Eur. J. Inorg. Chem.* 2013, 819– 831.

21 - 21aM. L. Scudder, H. A. Goodwin, I. G. Dance, *New J. Chem.* 1999, 23, 695– 705; 21bJ. McMurtrie, I. Dance, *CrystEngComm* 2005, 7, 216– 229; 21cJ. McMurtrie, I. Dance, *CrystEngComm* 2010, 12, 2700– 2710.

22 - 22aJ. K. McCusker, A. L. Rheingold, D. N. Hendrickson, *Inorg. Chem.* 1996, 35, 2100– 2112; 22bP. Guionneau, M. Marchivie, G. Bravic, J.-F. Létard, D. Chasseau, *Top. Curr. Chem.* 2004, 234, 97– 128.

23 J. M. Holland, J. A. McAllister, C. A. Kilner, M. Thornton-Pett, A. J. Bridgeman, M. A. Halcrow, *J. Chem. Soc. Dalton Trans.* 2002, 548– 554.

24 - 24aJ. Elhaik, D. J. Evans, C. A. Kilner, M. A. Halcrow, *Dalton Trans.* 2005, 1693– 1700; 24bC. A. Kilner, M. A. Halcrow, *Polyhedron* 2006, 25, 235– 240; 24cM. Haryono, F. W. Heinemann, K. Petukhov, K. Gieb, P. Müller, A. Grohmann, *Eur. J. Inorg. Chem.* 2009, 2136– 2143.

25 Additional crystallographic figures and tables, definitions of the structure parameters in Table 1, DSC and powder diffraction data are given in the Supporting Information.

26 L. Pauling, The Nature of the Chemical Bond, 3rd ed., Cornell University Press, Ithaca, New York, 1960, pp. 257– 264.

27 - 27aC. Carbonera, C. A. Kilner, J.-F. Létard, M. A. Halcrow, *Dalton Trans.* 2007, 1284– 1292; 27bC. A. Tovee, C. A. Kilner, J. A. Thomas, M. A. Halcrow, *CrystEngComm* 2009, 11, 2069– 2077.

28 - 28aC. Carbonera, J. S. Costa, V. A. Money, J. Elhaïk, J. A. K. Howard, M. A. Halcrow, J.-F. Létard, *Dalton Trans.* 2006, 3058– 3066; 28bG. Chastanet, C. A. Tovee, G. Hyett, M. A. Halcrow, J.-F. Létard, *Dalton Trans.* 2012, 41, 4896– 4902.

29 I. Šalitroš, O. Fuhr, R. Kruk, J. Pavlik, L. Pogány, B. Schäfer, M. Tatarko, R. Boča, W. Linert, M. Ruben, *Eur. J. Inorg. Chem.* 2013, 1049– 1057.

30 I. Šalitroš, L. Pogány, M. Ruben, R. Boča, W. Linert, *Dalton Trans.* 2014, 43, 16584– 16587.

31- 31aJ.-F. Létard, P. Guionneau, L. Rabardel, J. A. K. Howard, A. Goeta, D. Chasseau, O. Kahn, *Inorg. Chem.* 1998, 37, 4432– 4441; 31bS. Marcén, L. Lecren, L. Capes, H. A. Goodwin, J.-F. Létard, *Chem. Phys. Lett.* 2002, 358, 87– 95; 31cJ.-F. Létard, P. Guionneau, O. Nguyen, J. S. Costa, S. Marcen, G. Chastanet, M. Marchivie, L. Capes, *Chem. Eur. J.* 2005, 11, 4582– 4589; 31dJ.-F. Létard, G. Chastanet, P. Guionneau, C. Desplanches in Spin Crossover Materials—Properties and Applications (Ed.:), Wiley, Chichester, 2013, Chap. 19, pp. 475– 506.

32 J.-F. Létard, *J. Mater. Chem.* 2006, 16, 2550– 2559.

33 O. Kahn, Molecular Magnetism, VCH, Weinheim, 1993.

34 - 34aA. Hauser, *Coord. Chem. Rev.* 1991, 111, 275– 290; 34bA. Hauser, C. Enachescu, M. L. Daku, A. Vargas, N. Amstutz, *Coord. Chem. Rev.* 2006, 250, 1642– 1652.

35 A. Hauser, J. Jeftic, H. Romstedt, R. Hinek, H. Spiering, *Coord. Chem. Rev.* 1999, 190–192, 471– 491.

36 I. Krivokapic, C. Enachescu, R. Bronisz, A. Hauser, *Inorg. Chim. Acta* 2008, 361, 3616– 3622.

37 - 37aG. Chastanet, A. B. Gaspar, J. A. Real, J.-F. Létard, *Chem. Commun.* 2001, 819– 820; 37bG. Chastanet, C. Carbonera, C. Mingotaud, J.-F. Létard, *J. Mater. Chem.* 2004, 14, 3516– 3523.

38 - 38aV. Niel, A. L. Thompson, A. E. Goeta, C. Enachescu, A. Hauser, A. Galet, M. C. Munoz, J. A. Real, *Chem. Eur. J.* 2005, 11, 2047– 2060; 38bJ. Klingele, D. Kaase, M. Schmucker, Y. Lan, G. Chastanet, J. F. Létard, *Inorg. Chem.* 2013, 52, 6000– 6010; 38cC. Baldé, W. Bauer, E. Kaps, S. Neville, C. Desplanches, G. Chastanet, B. Weber, J. F. Létard, *Eur. J. Inorg. Chem.* 2013, 2744– 2750.

39 J.-F. Létard, G. Chastanet, O. Nguyen, S. Marcèn, M. Marchivie, P. Guionneau, D. Chasseau, P. Gütlich, *Monatsh. Chem.* 2003, 134, 165– 182.

40 - 40aA. Navrotsky, L. Mazeina, J. Majzlan, *Science* 2008, 319, 1635– 1638; 40bA. Navrotsky, *ChemPhysChem* 2011, 12, 2207– 2215; 40cB. D. Hamilton, J.-M. Ha, M. A. Hillmyer, M. D. Ward, *Acc. Chem. Res.* 2012, 45, 414– 423; 40dY. Sakata, S. Furukawa, M. Kondo, K. Hirai, N. Horike, Y. Takashima, H. Uehara, N. Louvain, M. Meilikhov, T. Tsuruoka, S. Isoda, W. Kosaka, O. Sakata, S. Kitagawa, *Science* 2013, 339, 193– 196; 40eC. Zhang, J. A. Gee, D. S. Sholl, R. P. Lively, *J. Phys. Chem. C* 2014, 118, 20727– 20733.

41 M. Mikolasek, G. Félix, W. Nicolazzi, G. Molnár, L. Salmon, A. Bousseksou, *New J. Chem.* 2014, 38, 1834– 1839.

42 - 42aJ. M. Crettez, E. Coquet, B. Michaux, J. Pannetier, J. Bouillot, P. Orlans, A. Nonat, J. C. Mutin, *Phys. B* 1987, 144, 277– 291; 42bF. Iwatsu, *J. Phys. Chem.* 1988, 92, 1678– 1681; 42cI. Yamashita, H. Kawaji, T. Atake, Y. Kuroiwa, A. Sawada, *Phys. Rev. B* 2003, 68, 092104.

43 - Particle-size effects can also be important in spin-crossover transitions, whether or not they involve a crystallographic phase change. See for example ref. [41], and: 43aE. W. Müller, H. Spiering, P. Gütlich, *Chem. Phys. Lett.* 1982, 93, 567; 43bE. Koenig, G. Ritter, S. K. Kulshreshtha, N. Csatary, *Inorg. Chem.* 1984, 23, 1903– 1910; 43cW. D. Federer, D. N. Hendrickson, *Inorg. Chem.* 1984, 23, 3870– 3877; 43dD. J. Rudd, C. R. Goldsmith, A. P. Cole, T. D. P. Stack, K. O. Hodgson, B. Hedman, *Inorg. Chem.* 2005, 44, 1221– 1229; 43eM. Sorai, R. Burriel, E. F. Westrum, Jr., D. N. Hendrickson, *J. Phys. Chem. B* 2008, 112, 4344; 43fC. Chong, A. Slimani, F. Varret, K. Boukheddaden, E. Collet, J.-C. Ameline, R. Bronisz, A. Hauser, *Chem. Phys. Lett.* 2011, 504, 29– 33.

44 I. Šalitroš, O. Fuhr, A. Eichhöfer, R. Kruk, J. Pavlik, L. Dlháň, R. Boča, M. Ruben, *Dalton Trans.* 2012, 41, 5163– 5171.

45 C. J. O'Connor, *Prog. Inorg. Chem.* 1982, 29, 203– 283.

46 *ChrysAlis Pro*, Oxford Diffraction Ltd, Abingdon, UK, **2006**.

47 G. M. Sheldrick, *Acta Crystallogr. Sect. A* 2008, 64, 112– 122.

48 L. J. Barbour, *J. Supramol. Chem.* 2001, 1, 189– 191.